Built-in biaxial strain dependence of Γ-X transport in GaAs/$In_xAl_{1-x}As$/GaAs pseudomorphic heterojunction barriers (x=0, 0.03, and 0.06)

K. Yang, J. R. East, and G. I. Haddad
Center for High Frequency Microelectronics, Department of Electrical Engineering and Computer Science, The University of Michigan, Ann Arbor, Michigan 48109-2122

T. J. Drummond, T. M. Brennan, and B. E. Hammons
Sandia National Laboratories, P.O. Box 5800, Albuquerque, New Mexico 87185-1370

(Received 12 May 1994; accepted for publication 26 August 1994)

The effects of built-in biaxial strain on Γ-X transport in n-GaAs/i-$In_xAl_{1-x}As$/n-GaAs pseudomorphic single-barrier structures (x=0, 0.03, and 0.06) are studied by measuring temperature-dependent I-V characteristics. For the accurate characterization of electron transport across each barrier, a self-consistent numerical model is used to analyze the experimental results. For each structure, the four barrier parameters defined from the thermionic-field-emission theory, the effective Richardson constant A^*, the conduction-band offsets $\Delta E_{c1,2}$, and a tunneling mass m_n^* are extracted by calculating the theoretical I-V characteristics and fitting them to the experimental I-V-T data. The experimentally obtained X-point conduction-band shifts with the addition of indium are compared with the theoretical results calculated based on the model-solid theory. The results indicate that the addition of indium not only splits the degenerate X minima of the $In_xAl_{1-x}As$ barrier, but also shifts the relative barrier heights of both longitudinal and transverse X valleys due to the alloy-dependent band-structure modification. The comparison between the experimental and theoretical results illustrates that the transverse X valleys are the main conduction channel for the Γ-X transport across $In_xAl_{1-x}As$ pseudomorphic barriers. © *1994 American Institute of Physics.*

I. INTRODUCTION

Recently, $Al_xGa_{1-x}As$/GaAs tunneling heterostructures have attracted considerable interest in view of their numerous potential device applications.[1–4] The investigations of these structures have demonstrated that the X-point energy plays a very important role in the electron transport when the conduction-band structure changes from the Γ point to the X point ($x \geq 0.45$).[5–13] The experimental study by Solomon and co-workers[5] on the I-V characteristics of n-GaAs/i-$Al_xGa_{1-x}As$/n-GaAs barriers with different aluminum mole fractions showed that the perpendicular electron transport across these barriers occurs through the Γ point for low Al fraction devices, but through the X point for high Al fraction devices.

For transport through the sixfold X valleys, lying in the (100) directions in the Brillouin zone, there are two different current paths, i.e., two longitudinal X valleys (X_l valley) aligned in the current direction with the Γ point at the zone center and four transverse X valleys (X_t valley). Although Beresford *et al.*[8] reported that a bound state associated with the X_l valleys of a single-barrier structure with a thin AlAs layer produces a negative differential resistance in the I-V characteristics, the role of X_l valleys has been found insignificant for the Γ-X transport through tunneling barriers with a thickness larger than 300 Å.[5,10,11] One way to clarify the complicated current conduction mechanisms through the sixfold degenerate X minima is uniaxial stress applied external to the sample to remove the X-point degeneracy. The analysis of the external stress-dependent I-V data based on the Fowler–Nordheim plot approach[11] has confirmed that the X_t valleys are more favored in electron transport through thick X barriers due to the fact that the effective mass of X_t valleys in the electron propagation direction ($\sim 0.19 m_0$) is much smaller than that of the X_l valleys ($\sim 1.1 m_0$). Furthermore, it was observed that the prefactors of thermionic emission and tunneling currents for the case of Γ-X transport are significantly smaller than those of Γ-Γ transport.[5,10,11] These facts indicate that the wave-function selection rules at the heterojunction interface play an important role in the perpendicular transport across the heterojunction barriers.

In this article biaxial-strain-dependent Γ-X transport in $In_xAl_{1-x}As$ pseudomorphic heterojunction barriers is studied by measuring temperature-dependent I-V characteristics. Three different n-GaAs/i-$In_xAl_{1-x}As$/n-GaAs heterostructures with indium mole fractions of 0, 0.03, and 0.06 were grown by molecular-beam epitaxy (MBE). Each structure has a 600-Å-thick tunneling barrier in which a different degree of internal biaxial compressive strain is generated according to the incorporated indium composition. The details of sample preparation and measurements are described in Sec. II. Theoretical methods used for the analysis of measured I-V-T data are presented in Sec. III. In Sec. IV, the experimental conduction-band shifts with biaxial strain are compared with the theoretical predictions based on the model-solid theory. The conclusions are given in Sec. V.

II. EXPERIMENT

A. Sample preparation

The samples described were prepared by MBE on (100)-oriented, heavily Si-doped n^+-GaAs substrates. Figure 1 shows a schematic diagram representing the structures used in the experiments. Starting with the substrate, the structure

 0021-8979/94/76(12)/7907/8/$6.00

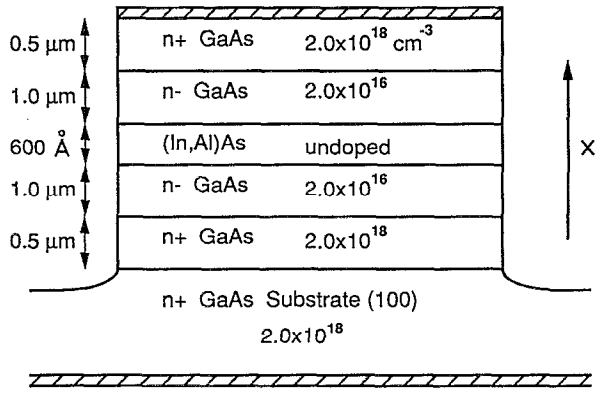

FIG. 1. Schematic diagram of the sample structure.

consisted of a 0.5 μm n^+ GaAs layer, a 1.0 μm n^- GaAs layer, an undoped 600 Å $In_xAl_{1-x}As$ barrier layer, a 1.0 μm n^- GaAs layer, and a 0.5 μm n^+ GaAs layer. Nominal values for x were 0, 0.03, and 0.06. The thickness and indium compositions of the barrier layer were selected to study the perpendicular transport process of thermionic-field emission across pseudomorphic InAlAs barriers under the built-in biaxial strain effects. The maximum amount of indium was determined considering the critical thickness of the material system.[15] The n^+ doping level was 2.0×10^{18} cm^{-3} and the n^- doping level was 2.0×10^{16} cm^{-3}. The dopant was Si throughout. The growth temperature was nominally 580 °C throughout the growth of the structure with the AlAs barrier. For the InAlAs barrier layer structures the growth temperature was lowered 15 °C (from the 580 °C used for the GaAs layers) for the growth of the barriers with the intent of suppressing indium segregation and reevaporation from the surface. The temperature adjustment was abrupt as possible within the response time limitation of the system. Growth interruptions were not employed to avoid possible accumulation of background contamination from the vacuum system ambient. Si doping levels were continuous up to each interface. Due to the low doping levels involved Si segregation effects should be negligible.

The samples were processed using standard photolithography and liftoff procedures. Circular 60- and 90-μm-diam mesa-isolated diodes were fabricated for each sample. Ni/Au/Ge/Ti/Au ohmic contacts were made to the back of the sample and to the top GaAs. In order to remove the effects of different processing conditions on the characterization of the properties of each heterostructure, all three samples were fabricated in parallel under the same processing conditions.

B. Measurement

The temperature-dependent I-V characteristics were measured with a HP 4145B parameter analyzer for samples mounted in a Joule–Thomson expansion-cooled cryostat that can maintain temperatures to ±1 K in the range 77–370 K. For all measurements the top contact was biased with respect to the substrate, which was held at ground potential. The reproducibility was confirmed by measuring consistent I-V characteristics over the device structures randomly selected across the wafer. For all samples, slight asymmetries were observed in the I-V characteristics despite the nominally symmetric structure. As discussed later this asymmetry is attributed to differences in the monolayer scale roughness at the two interfaces. At each temperature the current ratio of the two different diameter diodes was measured. For temperatures above ~200 K, the current ratio was verified to be the area ratio of the two different size diodes; however, at lower temperatures it was observed that the current ratio slightly deviates from the area ratio and varies to some extent from sample to sample, indicating the presence of locally distributed current conduction sources. The observation of this excess current at low temperatures has been reported for similar semiconductor-insulator-semiconductor (SIS) structures.[11,16,17] Impurity-assisted tunneling across the barrier or current conduction through the surface states has been considered as a possible source of the excess current.

For accurate characterization of barrier parameters under the relatively small built-in stress produced by the pseudomorphic growth, I-V-T data taken above 250 K were used for the analysis. In this temperature range, the transport across the barrier is dominated by thermionic processes and the large current conduction over the barrier will ensure the accuracy of parameters extracted based on the thermionic-field-emission theory.

The C-V characteristics were also measured at a temperature of 77 K with an HP4275A *LCR* meter to check the quality of the undoped InAlAs barrier layers. The measured C-V curves were symmetric and C-V shifts due to trapped charge at the barrier, which has been reported in similar structures,[18] were not observed in any of the samples.

III. THEORETICAL METHODS FOR THE ANALYSIS OF *I-V-T* DATA

A. Description of a numerical model

The total current density J at a temperature T across an InAlAs barrier is given by a sum of the current components which flow through several sets of nonequivalent valleys. For transport in the (100) direction, the current across the barrier is determined primarily by the current conduction through the X valleys. The contribution of a Γ-Γ transport process is not considered here because of the large barrier height of ~1 eV. Although there are two current channels of the longitudinal and transverse valleys for the Γ-X transport, the parameter extraction of electron transport across each barrier is performed based on the current expression given by Eq. (1) in which the two current paths through the X valleys are not separated. This is due to the fact that, even though two sets of parameters can be used to consider the two different X-valley channels for the data fitting, there is no way to determine uniquely a set of parameters among many possible combinations especially under the relatively weak built-in strain effects investigated here. Therefore, in this study only one set of barrier parameters is defined and used to characterize the overall electron transport through the sixfold degenerate X valleys. The total electron current flowing across a rectangular barrier located between $x=x_1$ and x_2, the first and second grown interfaces, is given by[19]

$$J=J_1-J_2=-\frac{A^*T}{k}\int D(E_x)\times\left\{\ln\left[1+\exp\left(\frac{E_f(x=x_1^-)-E_x}{kT}\right)\right]-\ln\left[1+\exp\left(\frac{E_f(x=x_2^+)-E_x}{kT}\right)\right]\right\}dE_x, \quad (1)$$

where A^* is the effective Richardson constant, k is the Boltzmann constant, $D(E_x)$ is the quantum-mechanical transmission probability, E_x is the energy of electrons in the current direction, and E_f is the Fermi level.

In order to obtain the conduction-band profile to calculate the conducting current across the barrier, Poisson's equation is solved,

$$\frac{d}{dx}\left(\epsilon\frac{d\psi}{dx}\right)=-q(N_D^+-n), \quad (2)$$

where ψ denotes the electrostatic potential, n is the electron density, and N_D^+ is the ionized donor density. For a parabolic band, the electron density is given by

$$n=N_cF_{1/2}[(E_c-E_f)/kT], \quad (3)$$

where N_c is the effective density of states in the conduction band and $F_{1/2}$ is the Fermi–Dirac integral of order 1/2. The ionized donor density is calculated from the charge neutrality using the following expression:

$$N_D^+=\frac{N_D}{1+g_D\exp[(E_f-E_c+E_D)/kT]}, \quad (4)$$

where N_D is the donor density, g_D is the ground-state degeneracy factor of the donor level, and E_D is the donor activation energy. As for Si in GaAs, g_D is 2 and E_D is 0.005 eV,[20] respectively.

The conventional calculation scheme solves Poisson's equation usually assuming that the Fermi level is flat in the cladding layers and varies only across the barrier.[21,22] Although this assumption has been widely used in a number of numerical calculations for low-bias cases, the assumption of flat Fermi levels in the cladding layers is questionable for device structures investigated here especially at high biases. In order to overcome this limitation and evaluate the current crossing the barrier in a self-consistent manner, both the current continuity and Poisson's equations are solved simultaneously. For this purpose, a current continuity equation is formulated by coupling the tunneling and thermionic emission processes across the barrier with the drift-diffusion processes in the cladding layers. The drift-diffusion current for the cladding regions is given by

$$J=\mu_n n\frac{dE_f}{dx}. \quad (5)$$

The use of the drift-diffusion transport scheme in the cladding layers makes it possible to calculate the Fermi level of the entire device structure self-consistently by conserving the current. Two-dimensional quantum-mechanical effects such as energy subbands in the accumulated region and the effects of hot electrons are neglected, because the device dimensions investigated here are much larger than the mean free path of electrons and the applied bias is not large enough to induce any significant quantum effects in the accumulated region. The two different transport schemes are coupled by boundary conditions for the thermionic-field-emission current across a rectangular (or more generally trapezoidal) barrier. Using the WKB approximation, the transmission probability for electrons at the barrier is expressed as follows:

$$D(E_x)=\begin{cases}\exp\left(-\frac{4\pi}{h}\int_{x_1}^{x_E}\{2m_n^*[E_c(x)-E_x]\}^{1/2}dx\right), & \text{if } E_{\min}\leq E_x<E_{\max},\\ 1, & \text{if } E_{\max}\leq E_x,\end{cases} \quad (6)$$

where h is Planck's constant, m_n^* is the electron tun neling mass, E_x is the energy of the conduction band at $x=x_E$ $(x_1\leq x_E\leq x_2)$, $E_{\min}=\max[E_c(x_1^-),E_c(x_2^+)]$, and $E_{\max}=\max[E_c(x_1^+),E_c(x_2^-)]$. Using the Boltzmann distribution for the electrons going over the barrier by thermionic-field emission, since energies are more than a few kT above the Fermi level, the current flux injected from the left-hand side of the barrier for the forward bias case is expressed from Eq. (1) as

$$J_1=-A^*T^2(1+\delta)\exp\left(-\frac{\Delta E_{c1}}{kT}\right)\exp\left(\frac{E_f(x_1^-)-E_c(x_1^-)}{kT}\right), \quad (7)$$

where

$$\delta=\frac{\exp[E_c(x_1^+)/kT]}{kT}\times\int_{E_c(x_1^-)}^{E_c(x_1^+)}\exp\left(-\frac{4\pi}{h}\int_{x_1}^{x_E}\{2m_n^*[E_c(x)-E_x]\}^{1/2}dx\right)\exp\left(-\frac{E_x}{kT}\right)dE_x. \quad (8)$$

A similar derivation yields the following equation for the opposing flux:

$$J_2 = -A^*T^2(1+\delta)\exp\left(-\frac{\Delta E_{c2}+qV_b}{kT}\right)$$
$$\times\exp\left(\frac{E_f(x_2^+)-E_c(x_2^+)}{kT}\right), \quad (9)$$

where V_b denotes the potential drop across the InAlAs barrier for a given bias. Expressions for J_1 and J_2 under reverse bias also can be derived in a similar fashion. The contribution of tunneling is formulated through a parameter δ being evaluated from the conduction-band profile and a tunneling mass m_n^* based on Eq. (8). As can be seen from Eqs. (7) and (9), the electron transport across a trapezoidal barrier is characterized by the four parameters of A^*, ΔE_{c1}, ΔE_{c2}, and m_n^*. Except for these four parameters, all the other quantities such as the Fermi level (or electron density) and electrostatic potential are self-consistently determined throughout the structure. By implementing the electron fluxes over the barrier represented by Eqs. (7) and (9) as boundary conditions at the heterointerfaces on the one-dimensional drift-diffusion numerical scheme represented by Eq. (5), the current continuity and Poisson's equations are simultaneously solved. The details of calculation procedures can be found in Ref. 23. The self-consistently calculated Fermi level at $T=300$ K at a bias of -0.8 V is shown in Fig. 2 for a device structure illustrated in Fig. 1. When the applied bias is less than 0.6 V, the Fermi levels in the cladding layers have been found to be nearly constant; however, when the applied bias exceeds 0.6 V for the temperature range investigated here, the Fermi level is observed to bend in the depleted region as shown in Fig. 2.

In the present study, the numerical model described above is used to calculate the theoretical I-V characteristics and to fit them to the measured I-V data. The four parameters A^*, ΔE_{c1}, ΔE_{c2}, and m_n^* are used as fitting parameters. The slight asymmetry in the I-V characteristics is modeled by replacing the ideal rectangular barrier with equal Γ-X offsets by a trapezoidal barrier with the two different offsets, ΔE_{c1} and ΔE_{c2}. The device structure shown in Fig. 1 is used in the simulation including the heavily doped n^+ layers except only for the thick substrate. The material parameters used in this calculation are taken from Ref. 24. The temperature dependence of energy band gap and electron mobility also have been taken into account.[23] The detail parameter extraction procedures and results of the data fitting are discussed in the following subsection.

B. Analysis of I-V-T data

The analysis of measured I-V-T data begins with finding the barrier activation energies $\Delta E_{c1,2}^*$ and the prefactor A^{**} from the conventional approach based on the Arrhenius plot of $\ln(J/T^2)$ vs $1/T$.[5,10,11,25] These values are then used as initial guesses for the data fitting based on the numerical approach described in the previous subsection.

Under a relatively small bias over the temperature range investigated here, the current conduction across the InAlAs barrier is primarily determined by thermionic emission of electrons. When the magnitude of the applied bias is greater than a few kT/q, the electron flux from one direction in Eq. (1) dominates the other depending on the bias polarity. Under this condition, rearranging Eq. (7) yields the following expression for the forward bias case:

$$\ln(J/T^2)+\eta(T)=\ln(A^{**})-\Delta E_{c1}^*/kT, \quad (10)$$

where η represents the separation between the conduction-band edge and the Fermi level in the quasineutral region, and A^{**} and ΔE_{c1}^* denote the prefactor and the activation energy seen from the emitter side. It should be noted that the prefactor and the activation energy in the above equation are functions of applied bias and are different from the effective Richardson constant A^* and the conduction-band offset ΔE_c defined in the previous subsection. By plotting $\ln(J/T^2)+\eta(T)$ vs $1/T$ at each bias, the activation energy and the prefactor are obtained from the slope and the intercept at $1/T=0$ of the Arrhenius plot as a function of applied bias using a least-squares-fitting algorithm. The Arrhenius plots and the corresponding prefactors and activation energies obtained for an $In_{0.03}Al_{0.97}As$ barrier are shown in Fig. 3. The values of A^{**} and ΔE_c^* that are extrapolated to zero bias are usually considered as the effective Richardson constant A^* and the conduction-band barrier height ΔE_c. Although this scheme of parameter extraction has been widely used because of its simplicity, some care is required for the accurate characterization of barrier parameters. Even though the effects of band bending on A^{**} and ΔE_c^* are removed by extrapolating them to the flatband case, the fact that Eq. (10) is strictly valid only when the applied voltage is greater than a few kT/q limits the accuracy of this simple method. The strong bias dependence of the prefactor observed in Fig. 3(c) for the bias range below a few kT/q makes the accurate determination of A^* difficult. The value of A^* obtained from the prefactor at a small bias close to the flatband condition can significantly underestimate its true value. In addition,

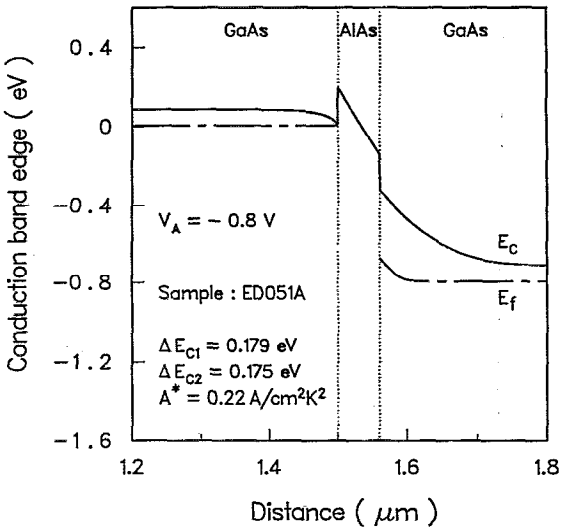

FIG. 2. Conduction-band edge E_c and Fermi level E_f of a GaAs/AlAs/GaAs heterojunction barrier at a bias of -0.8 V at $T=300$ K. The numerical technique described in Sec. III is applied in this calculation.

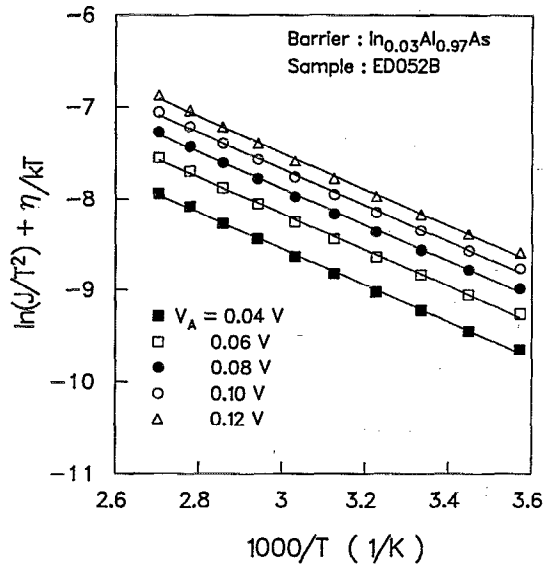

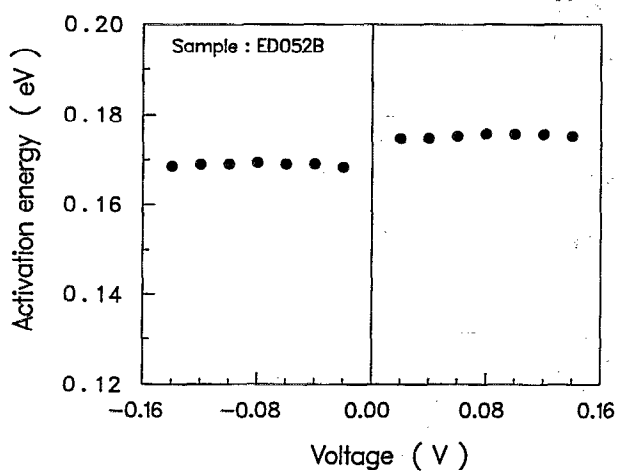

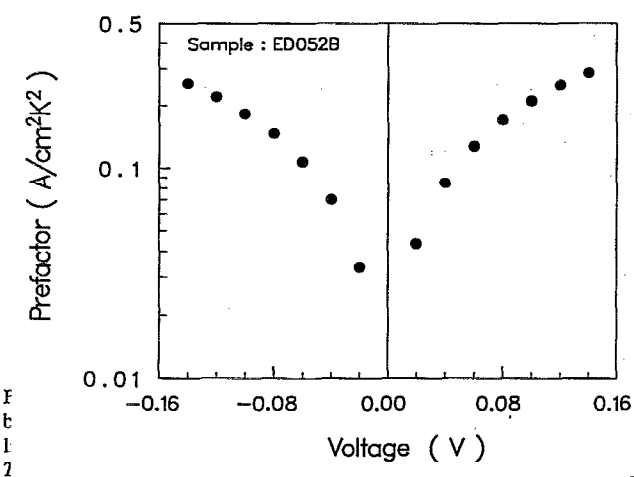

voltage.

neglecting the temperature dependence of the opposing flux introduces another source of uncertainty in the parameter extraction.

To overcome these difficulties found in the conventional extrapolation scheme, the full I-V characteristics are used in the analysis. By employing the numerical model described in

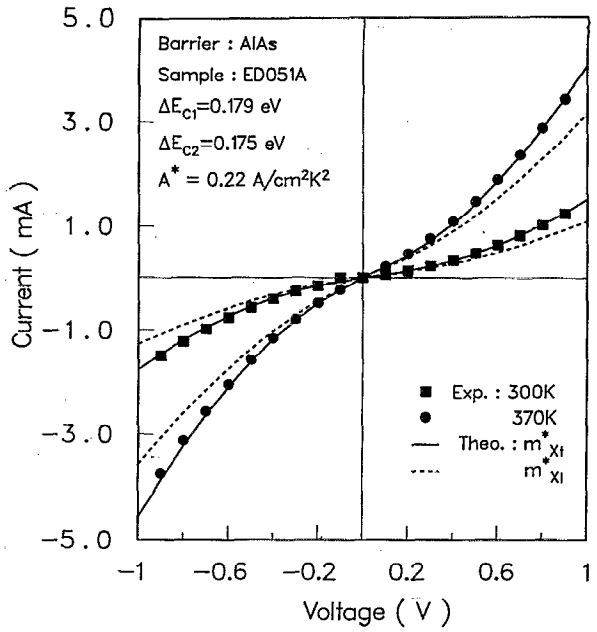

FIG. 4. The I-V characteristics of an AlAs barrier calculated using a tunneling mass of $m^*_{X_t} = 0.19m_0$ (solid line) and $m^*_{X_l} = 1.1m_0$ (dashed line). The experimental I-V data at T=300 and 370 K are shown by squares and circles, respectively.

the previous subsection, the I-V characteristics are calculated as a function of temperature and fitted to the experimental I-V data measured over the bias range from -1 to 1 V (-0.5 to 0.5 V in some cases depending on the data) at temperatures above 250 K by varying the four parameters of A^*, ΔE_{c1}, ΔE_{c2}, and m_n^*. For the tunneling mass m_n^*, the two different values of $0.19m_0$ for the transverse X valleys and $1.1m_0$ for the longitudinal X valleys of AlAs (Ref. 26) are used during the fitting procedures for all three barriers. This assumes that these effective masses are not modified significantly under the weak biaxial strain effects. Although the actual tunneling masses below the band edge are typically less than the band-edge effective masses,[27,28] these effects are considered to be small in this study due to the thick tunneling barriers.[5,11] One important fact found through these fitting procedures is that the data fitting can be achieved only with the lighter mass of $0.19m_0$. The use of a heavy longitudinal mass for the tunneling mass leads to a considerable underestimation of tunneling contribution to the total current, whereas the transverse mass of $0.19m_0$ gives an excellent fit to experiment results as shown in Fig. 4. The results partly illustrate that the transverse X valleys are more favored between the two different X valleys as was revealed by Fowler–Nordheim tunneling studies in earlier works.[5,11] This issue is discussed further in the next section when the obtained band-edge shifts of the conduction band under built-in biaxial strain are compared with the theoretical results.

Starting with the parameter values obtained from the Arrhenius plot method and the transverse mass of $0.19m_0$ as a tunneling mass, the experimental I-V characteristics measured at each temperature are fitted. At first, A^* is varied while keeping the barrier heights constant. After obtaining a value of A^* that gives the best fit to the experimental data

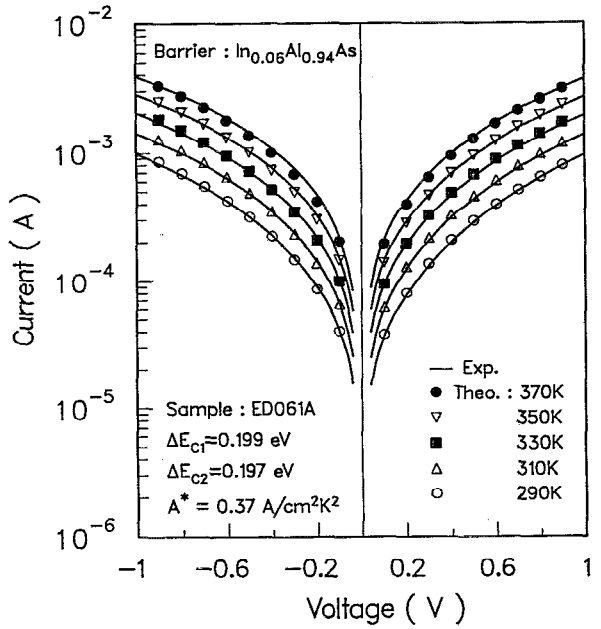

FIG. 5. Theoretical and experimental I-V characteristics at different temperatures of a GaAs/$In_{0.06}Al_{0.94}As$/GaAs heterojunction barrier.

with fixed barrier heights, the values of ΔE_{c1} and ΔE_{c2} are updated based on the error between the theoretical and experimental results. These procedures continue until the standard variation between the experimental and calculated results is minimized. The fact that a slight variation of the conduction-band offset has a significant impact on the I-V-T characteristics ensures the accuracy of the extracted values of ΔE_{c1} and ΔE_{c2} within an error margin of about ± 2 meV. Figure 5 shows the theoretical I-V characteristics fitted to the experimental data for an $In_{0.06}Al_{0.94}As$ barrier. For each barrier, the I-V-T data of two different diodes were analyzed and the extracted values of A^*, ΔE_{c1}, and ΔE_{c2} are summarized in Table I. As is seen for the case of sample ED052B [Fig. 3(b) and Table I], the barrier heights obtained based on the full analysis are slightly larger than the activation energies extracted from the Arrhenius plot analysis. For all samples the I-V characteristics were slightly asymmetric despite the nominally symmetric device structure. The asymmetry could be due to several different effects: dopant diffusion, Ga and/or In surface segregation, or differences in the length scale of the interfacial roughness affecting Γ-X scattering rates. At a doping level of 10^{16} cm^{-3} movement of the Si is considered unlikely. Segregation of Ga and/or In is more likely to produce the observed effect, however, the degree of asymmetry is essentially independent of In concentration which should be expected to segregate the most strongly.[29,30] Finally, if one considers the length scale of the surface roughness to be a relevant factor it should be expected that the GaAs-to-AlAs interface should have larger regions of monolayer planarity than the AlAs-to-GaAs surface due to the higher surface mobility of Ga atoms as compared to Al atoms. Al atoms should control interface roughness for low In fractions as well as for pure AlAs. The rougher InAlAs-to-GaAs interface might be expected to enhance the direct to indirect scattering rate and lower the apparent barrier height consistently in all cases. Taking the values of ΔE_{c1} as conduction-band offsets for the corresponding heterostructures, it is found that the conduction-band offset increases linearly by 10 meV per 3% increase of indium composition. The conduction-band discontinuity of the AlAs barrier obtained here is in good agreement with the values reported by other authors[25,31] within the indicated experimental error range. The observed increase of A^* with the indium addition as shown in Table I indicates that the overall electron transport is enhanced with an increase of splitting between the X_t and X_l valleys even though the barrier heights associated with both valleys are actually increasing.

In order to achieve further understanding on the experimentally characterized strain effects, a theoretical calculation of strain-dependent band-edge shifts is performed based on the model-solid theory[14] in the following section.

IV. BAND-EDGE SHIFTS UNDER BUILT-IN BIAXIAL STRAIN IN $In_xAl_{1-x}As$ PSEUDOMORPHIC LAYERS

To study the band-edge shifts under biaxial strain of $In_xAl_{1-x}As$ pseudomorphic to a GaAs substrate, three factors need to be considered: first, alloy-induced changes in band gap and offset; second and third, the hydrostatic and uniaxial components of strain, respectively.

To account for the alloy effects in $In_xAl_{1-x}As$ with the inclusion of indium, the material parameters of $In_xAl_{1-x}As$ are determined from known values of each alloy by the interpolation scheme. The material parameters of InAs, AlAs, and GaAs used in the calculation are summarized in Table II. The listed parameters show the values at $T=300$ K. The linear interpolation approximation was used for all the alloy parameters except for the energy levels of the X-point conduction band E_g^X and the average valence band $E_{v,\mathrm{avg}}$, which is used as an energy reference in the model-solid theory.[14] The bowing of E_g^X with the addition of indium is taken into account by a bowing parameter of 0.129 eV.[32] The nonlinear behavior of $E_{v,\mathrm{avg}}$ in $In_xAl_{1-x}As$ alloys is considered in this calculation by adopting a theoretical expression suggested in Ref. 14.

For biaxial strain along in-plane [100] directions, the shifts and splittings of the X-point conduction bands due to the hydrostatic and biaxial compression in a pseudomorphic $In_xAl_{1-x}As$ layer are calculated as follows:[33]

TABLE I. Extracted barrier parameters of GaAs/$In_xAl_{1-x}As$/GaAs pseudomorphic heterojunction barriers.

Indium mole fraction	Sample No.	ΔE_{c1} (eV)	ΔE_{c2} (eV)	A^* (A/cm^2 K^2)
0.0	ED051A	0.179	0.175	0.22
	ED051B	0.179	0.175	0.24
0.03	ED052A	0.189	0.185	0.33
	ED052B	0.189	0.185	0.32
0.06	ED061A	0.199	0.197	0.37
	ED061B	0.200	0.193	0.30

$$\Delta X_h = 2\Xi_{X_h}(1 - C_{12}/C_{11})e_{\parallel} \tag{11}$$

$$\Delta X_s = \Delta X_l - \Delta X_t = -\Xi_{X_s}(1 + 2C_{12}/C_{11})e_{\parallel}, \tag{12}$$

$$\Delta X_t = -\tfrac{1}{3}\Delta X_s, \tag{13}$$

$$\Delta X_l = \tfrac{2}{3}\Delta X_s, \tag{14}$$

where $e_{\parallel}$ is the parallel strain in $In_xAl_{1-x}As$,

$$e_{\parallel} = -\frac{a_x - a_0}{a_x}, \tag{15}$$

which is determined by the lattice constant of GaAs, a_0, and that of $In_xAl_{1-x}As$, a_x. Here, ΔX_h is the hydrostatic component of the biaxial compression, ΔX_s is the shear component, and ΔX_t and ΔX_l are the split shear components for the X_t valleys and the X_l valleys, respectively. C_{11} and C_{12} represent the elastic stiffness constants and Ξ_{X_h} and Ξ_{X_s} denote the hydrostatic and shear deformation potentials, respectively. The 1/3, 2/3 splitting of X valleys conserves the center of mass of the density of states.

The shifts of the Γ-point valence bands are obtained as follows:

$$\Delta V_h = 2\Xi_{vh}(1 - C_{12}/C_{11})e_{\parallel}, \tag{16}$$

$$\Delta V_{HH} = \tfrac{1}{3}\Delta_0 - \tfrac{1}{2}\delta E_{001}, \tag{17}$$

$$\Delta V_{LH} = -\tfrac{1}{6}\Delta_0 + \tfrac{1}{4}\delta E_{001} + \tfrac{1}{2}[\Delta_0^2 + \Delta_0\delta E_{001} + \tfrac{9}{4}(\delta E_{001})^2]^{1/2}, \tag{18}$$

$$\Delta V_{SO} = -\tfrac{1}{6}\Delta_0 + \tfrac{1}{4}\delta E_{001} - \tfrac{1}{2}[\Delta_0^2 + \Delta_0\delta E_{001} + \tfrac{9}{4}(\delta E_{001})^2]^{1/2}, \tag{19}$$

where

$$\delta E_{001} = -2\Xi_{vs}(1 + 2C_{12}/C_{11})e_{\parallel}. \tag{20}$$

Here ΔV_h is the hydrostatic component of the biaxial compression and ΔV_{HH}, ΔV_{LH}, and ΔV_{SO} are the split shear components for the heavy hole, the light hole, and the split-off bands, respectively. Δ_0 is the spin-orbit splitting and Ξ_{vh} and Ξ_{vs} denote the hydrostatic and shear deformation potentials for the valence bands, respectively.

By considering all the changes induced by alloy and biaxial strain, the overall shifts of the band edges for both conduction and valence bands are calculated based on the model-solid theory.[14] In order to confirm the reliability of this model, the experimentally observed lineups in closely related systems of GaAs/AlAs and $In_{0.52}Al_{0.48}As/In_{0.53}Ga_{0.47}As$ were first evaluated prior to calculating the behavior of the X-point energy in pseudomorphic $In_xAl_{1-x}As$. To fit the experimental values of ΔE_v of 0.55 eV (Ref. 25) for GaAs/AlAs and 0.2 eV (Ref. 34) for $In_{0.52}Al_{0.48}As/In_{0.53}Ga_{0.47}As$, the reference energy $E_{v,avg}$ of AlAs, which is found to be the most critical in the band lineup calculations of the corresponding material systems, was modified from a value of -7.49 eV (Ref. 14) to -7.45 eV. This new reference value gives the best results of 0.54 and 0.2 eV for the valence-band offsets, respectively.

In the calculation of a band-structure modification in $In_xAl_{1-x}As$, the value of -7.45 eV was used for $E_{v,avg}$ of AlAs. For the other parameters, the values listed in Table II were used. Figure 6 shows the theoretical movement of the X-point conduction-band edges of pseudomorphic $In_xAl_{1-x}As$ with respect to the Γ-point conduction band of GaAs as a function of indium mole fraction. The experimental results obtained in the previous section are also compared. As is shown, the addition of indium gives rise to two significant effects on the conduction-band shifts. First, the biaxial strain built into $In_xAl_{1-x}As$ barriers splits the band edges of X_t and X_l further with an increase of indium composition. Second, both the transverse and longitudinal X valleys move up due to the upward shift of the reference level of $E_{v,avg}$ as the indium mole fraction increases. The experimentally determined conduction-band offsets are observed to increase as well with the increase of indium composition and follow the trend of transverse X valleys. This fact illustrates that the transverse valleys of the X point are indeed the dominant conduction channel for the electron transport across pseudomorphic $In_xAl_{1-x}As$ barriers under the built-in

TABLE II. Material parameters of GaAs, AlAs, and InAs used in the band-edge shift calculations.

Parameter	GaAs	AlAs	InAs
a (Å)	5.6535[a]	5.6622[b]	6.0585[a]
C_{11} (10^{11} dyn/cm^2)	11.904[c]	11.63[d]	8.663[c]
C_{12} (10^{11} dyn/cm^2)	5.378[c]	5.76[d]	4.848[c]
E_g^{Γ} (eV)	1.422[e]	3.03[f]	0.35[g]
E_g^{X} (eV)	1.9[h]	2.153[f]	1.9[i]
$E_{v,avg}$ (eV)	-6.92[j]	-7.45[k]	-6.67[j]
Δ_0 (eV)	0.341[e]	0.30[i]	0.371[g]
Ξ_{X_h} (eV)		3.65[m]	3.65[n]
Ξ_{X_s} (eV)	6.5[o]	5.8[p]	4.5[j]
Ξ_{vh} (eV)	1.16[j]	2.47[j]	1.0[j]
Ξ_{vs} (eV)	-1.7[j]	-2.0[q]	-1.8[j]

[a]G. Von Giesecke and H. Pfister, Acta Crystallogr. **11**, 368 (1958).
[b]M. S. Goorsky, T. F. Kuech, M. A. Tischler, and R. M. Potemski, Appl. Phys. Lett. **59**, 2269 (1991); B. K. Tanner, A. G. Turnbull, C. R. Stanley, A. H. Kean, and M. McElhinney, Appl. Phys. Lett. **59**, 2272 (1991).
[c]D. Swyt, Report No. C00-623-167, National Technical Information Service, Springfield, VA.
[d]S. M. Kikkarin, A. V. Tsarev, V. V. Shashkin, and I. B. Yakovkin, Sov. Phys. Solid State **30**, 1689 (1988).
[e]J. S. Blakemore, J. Appl. Phys. **53**, R123 (1982).
[f]B. Monemar, Phys. Rev. B **8**, 5711 (1973).
[g]F. Lukes, Phys. Status Solidi B **84**, K113 (1977).
[h]Reference 24.
[i]W. Drube, D. Straub, and F. J. Himpsel, Phys. Rev. B **35**, 5563 (1987).
[j]Reference 14.
[k]Adjusted from the value of -7.49 eV in Ref. 14 to fit the experimentally obtained ΔE_v for AlAs/GaAs and $In_{0.52}Al_{0.48}As/In_{0.53}Ga_{0.47}As$ material systems.
[l]Reference 26.
[m]Obtained from the deformation potential of E_g^X of AlAs, 1.18 eV, taken from K. Reimann, M. Holtz, K. Syassen, Y. C. Lu, and E. Bauser, Phys. Rev. B **44**, 2985 (1991), by adding Ξ_{vh}=2.47 eV of AlAs from Ref. 14.
[n]Assumed similar to AlAs.
[o]D. N. Mirlin, V. F. Sapega, I. Y. Karlik, and R. Katilius, Solid State Commun. **61**, 799 (1987).
[p]S. Charbonneau, J. F. Young, P. T. Coleridge, and B. Kettles, Phys. Rev. B **44**, 8312 (1991).
[q]Obtained from the data of S. Logothetidis, M. Cardona, L. Tapfer, and E. Bauser, J. Appl. Phys. **66**, 2108 (1989), using C_{11} and C_{12} of S. M. Kikkarin, A. V. Tsarev, V. V. Shashkin, and I. B. Yakovkin, Sov. Phys. Solid State **30**, 1689 (1988).

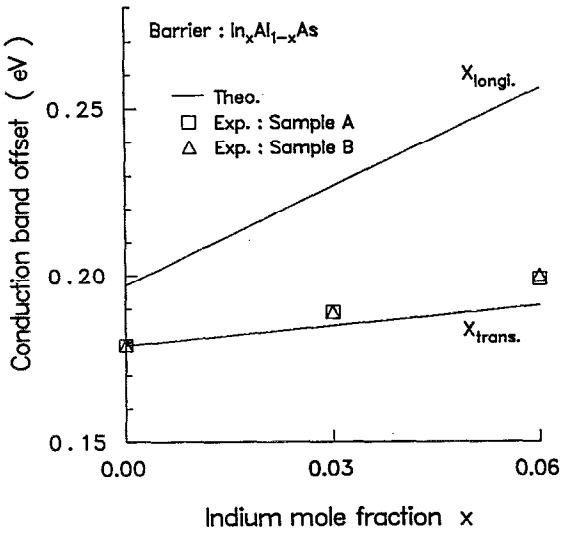

FIG. 6. Movement of the X-point conduction-band edges as a function of indium mole fraction. Two solid lines represent theoretical shifts of the band edges of longitudinal and transverse X valleys. The extracted barrier heights from samples A and B of each barrier are shown by squares and triangulars, respectively.

biaxial effects, which was indirectly revealed by a tunneling mass of $m_{X_t}^*$ in the previous fitting procedures.

V. CONCLUSION

The I-V characteristics of GaAs/$In_xAl_{1-x}As$/GaAs pseudomorphic barriers with indium mole fractions of 0, 0.03, and 0.06 were measured as a function of temperature and analyzed to characterize the electron transport via the X valleys under the effects of internally generated biaxial strain.

For the accurate determination of barrier parameters, the full I-V characteristics across each barrier were calculated by employing a self-consistent numerical model and the measured I-V-T data were fitted by varying the parameters of A^*, $\Delta E_{c1,2}$, and m_n^*. The conduction-band offset was found to increase linearly by 10 meV per 3% increase of indium composition. The comparison between the experimental and theoretical band-edge shifts shows that the small tunneling mass and the low barrier height associated with the transverse X valleys make the electron propagation through this channel more efficient than that via the longitudinal X valleys. The enhanced total conduction capability with the indium addition, reflected as the increase of A^*, indicates that the intervalley scattering between the six equivalent X valleys plays a significant role in the overall Γ-X transport processes.

ACKNOWLEDGMENTS

The work at the University of Michigan was supported by the U.S. Army Research Office under the URI program Grant No. DAAL03-92-G-0109. The work performed at Sandia National Laboratories was sponsored by the U.S. Department of Energy under Contract No. DE-AC04-94AL85000.

[1] L. L. Chang, L. Esaki, and R. Tsu, Appl. Phys. Lett. **24**, 593 (1974).
[2] S. Luryi, Appl. Phys. Lett. **47**, 490 (1985).
[3] T. C. L. G. Sollner, E. R. Brown, W. D. Goodhue, and H. Q. Le, Appl. Phys. Lett. **50**, 332 (1987).
[4] H. C. Liu and D. D. Coon, Appl. Phys. Lett. **50**, 1246 (1987).
[5] P. M. Solomon, S. L. Wright, and C. Lanza, Superlattices and Microelectronics **2**, 521 (1986).
[6] P. J. Price, Surf. Sci. **196**, 394 (1988).
[7] E. E. Mendez, E. Calleja, and W. I. Wang, Appl. Phys. Lett. **53**, 977 (1988).
[8] R. Beresford, L. F. Luo, W. I. Wang, and E. E. Mendez, Appl. Phys. Lett. **55**, 1555 (1989).
[9] D. Landheer, H. C. Liu, M. Buchanan, and R. Stoner, Appl. Phys. Lett. **54**, 1784 (1989).
[10] C. S. Kyono, V. P. Kesan, D. P. Neikirk, C. M. Maziar, and B. G. Streetman, Appl. Phys. Lett. **54**, 549 (1989).
[11] S. S. Lu, K. R. Lee, K. H. Lee, and M. I. Nathan, J. Appl. Phys. **67**, 6360 (1990).
[12] M. Rossmanith, J. Leo, and K. von Klitzing, J. Appl. Phys. **69**, 3641 (1991).
[13] J. P. Sun, R. K. Mains, K. Yang, and G. I. Haddad, J. Appl. Phys. **74**, 5053 (1993).
[14] C. G. Van de Walle, Phys. Rev. B **39**, 1871 (1989).
[15] T. G. Anderson, Z. G. Chen, V. D. Kulakovskii, A. Uddin, and J. T. Vallin, Appl. Phys. Lett. **51**, 752 (1987).
[16] D. Arnold, A. Ketterson, T. Henderson, J. Klem, and H. Morkoç, J. Appl. Phys. **57**, 2880 (1985).
[17] A. R. Bonnefoi, D. H. Chow, T. C. McGill, R. D. Burnham, and F. A. Ponce, J. Vac. Sci. Technol. B **4**, 988 (1986).
[18] T. W. Hickmott and P. M. Solomon, J. Appl. Phys. **57**, 2844 (1985).
[19] C. B. Duke, *Tunneling in Solids* (Academic, New York, 1969), p. 59.
[20] N. Chand, T. Henderson, J. Klem, W. T. Masselink, R. Fischer, Y. C. Chang, and H. Morkoç, Phys. Rev. B **30**, 4481 (1984).
[21] A. R. Bonnefoi, D. H. Chow, and T. C. McGill, J. Appl. Phys. **62**, 3836 (1987).
[22] B. Zimmermann, E. Marclay, M. Hegems, and P. Gueret, J. Appl. Phys. **64**, 3581 (1988).
[23] K. Yang, J. R. East, and G. I. Haddad, Solid-State Electron. **36**, 321 (1993).
[24] H. C. Casey, Jr. and M. B. Panish, *Heterostructure Lasers* (Academic, New York, 1978).
[25] J. Batey and S. L. Wright, J. Appl. Phys. **59**, 200 (1986).
[26] S. Adachi, J. Appl. Phys. **58**, R1 (1985).
[27] J. N. Schulman and Y. C. Chang, Phys. Rev. B **24**, 4445 (1981).
[28] G. Brozak, F. DeRosa, D. M. Hwang, P. Miceli, S. A. Schwartz, J. P. Harbison, L. T. Florez, and S. J. Allen, Jr., Surf. Sci. **229**, 493 (1990).
[29] W. Braun and K. H. Ploog, J. Appl. Phys. **75**, 1993 (1994).
[30] J. Nagle, J. P. Landesman, M. Larive, C. Mottet, and P. Bois, J. Cryst. Growth **127**, 550 (1993).
[31] E. E. Mendez, E. Calleja, and W. I. Wang, Phys. Rev. B **34**, 6026 (1986).
[32] The bowing parameter was determined by a quadratic fit of $E_g^X(x)$ to a crossover energy between $E_g^\Gamma(x)$ and $E_g^X(x)$ of $In_xAl_{1-x}As$ reported by M. R. Lorenz and A. Onton, in Proceedings of the 10th International Conference on the Physics of Semiconductors, 1970, p. 444.
[33] T. J. Drummond, E. D. Jones, H. P. Hjalmarson, and B. L. Doyle, Proc. SPIE, **796**, 2 (1987).
[34] R. People, K. W. Wecht, K. Alavi, and A. Y. Cho, Appl. Phys. Lett. **43**, 118 (1983).